

Enhanced xylene sensing performance of hierarchical flower-like Co_3O_4 via In doping

Jing Zhang(张京), Jianyu Ling(凌剑宇), Kuikun Gu(谷魁坤),Georgiy G. Levchenko, and Xiao Liang(梁霄)
Citation: Chin. Phys. B, 2023, 32 (**6**): 068104. DOI: 10.1088/1674-1056/acbe30
Journal homepage: http://cpb.iphy.ac.cn; http://iopscience.iop.org/cpb

What follows is a list of articles you may be interested in

High-sensitivity refractive index sensors based on Fano resonance in a metal-insulator-metal based arc-shaped resonator coupled with a rectangular stub

Shubin Yan(闫树斌), Hao Su(苏浩), Xiaoyu Zhang(张晓宇), Yi Zhang(张怡), Zhanbo Chen(陈展博), Xiushan Wu(吴秀山), and Ertian Hua(华尔天)
Chin. Phys. B, 2022, 31 (**10**): 108103. DOI: 10.1088/1674-1056/ac76ac

SnO_2/Co_3O_4 nanofibers using double jets electrospinning as low operating temperature gas sensor

Zhao Wang(王昭), Shu-Xing Fan(范树兴), and Wei Tang(唐伟)
Chin. Phys. B, 2022, 31 (**2**): 028101. DOI: 10.1088/1674-1056/ac1336

Tunable and highly sensitive temperature sensor based on graphene photonic crystal fiber

Xu Cheng(程旭), Xu Zhou(周旭), Chen Huang(黄琛), Can Liu(刘灿), Chaojie Ma(马超杰), Hao Hong(洪浩), Wentao Yu(于文韬), Kaihui Liu(刘开辉), and Zhongfan Liu(刘忠范)
Chin. Phys. B, 2021, 30 (**11**): 118103. DOI: 10.1088/1674-1056/ac11d0

Synaptic plasticity and classical conditioning mimicked in single indium-tungsten-oxide based neuromorphic transistor

Rui Liu(刘锐), Yongli He(何勇礼), Shanshan Jiang(姜珊珊), Li Zhu(朱力), Chunsheng Chen(陈春生), Ying Zhu(祝影), and Qing Wan(万青)
Chin. Phys. B, 2021, 30 (**5**): 058102. DOI: 10.1088/1674-1056/abc163

High sensitive pressure sensors based on multiple coating technique

Rizwan Zahoor, Chang Liu(刘畅), Muhammad Rizwan Anwar, Fu-Yan Lin(林付艳), An-Qi Hu(胡安琪), Xia Guo(郭霞)
Chin. Phys. B, 2020, 29 (**2**): 028102. DOI: 10.1088/1674-1056/ab6721

Enhanced xylene sensing performance of hierarchical flower-like Co_3O_4 via In doping

Jing Zhang(张京)[1], Jianyu Ling(凌剑宇)[1], Kuikun Gu(谷魁坤)[1], Georgiy G. Levchenko[1,3], and Xiao Liang(梁霄)[1,2,†]

[1] *State Key Laboratory of Superhard Materials, Physics of College, Jilin University, Changchun* 130012, *China*
[2] *Institute for Interdisciplinary Biomass Functional Materials Studies, Jilin Provincial Key Laboratory of Straw-Based Functional Materials, Jilin Engineering Normal University, Changchun* 130052, *China*
[3] *Donetsk Institute for Physics and Engineering named after O.O. Galkin, NAS of Ukraine, Kyiv* 03028, *Ukraine*

(Received 25 November 2022; revised manuscript received 29 January 2023; accepted manuscript online 23 February 2023)

Metal ions doping is a typical approach for tuning sensing properties of metal oxide semiconductors based gas sensors. Herein, hierarchical flower-like pure and In-doped Co_3O_4 nanostructures assembled by porous two-dimensional (2D) nanosheets are synthesized via a solvothermal method and annealing process. The sensing measurements display that the In@Co_3O_4-4 based sensor possesses high response value of 55.9 toward 100 ppm xylene at 150 °C, which is nearly 3.8 times larger than that of pure Co_3O_4 sensor. Furthermore, it possesses good selectivity and anti-humidity properties. Combined with the results of DFT calculations, the mechanism of enhanced gas sensing performance is analyzed systematically.

Keywords: sensor, Co_3O_4, xylene, density functional theory (DFT)

PACS: 81.07.–b, 07.07.Df **DOI:** 10.1088/1674-1056/acbe30

1. Introduction

As an important volatile organic compound (VOC), xylene is inevitably released from industrial wastes, cigarette smoke, various kinds of adhesives and so on.[1–3] In addition, it is harmful to the environment and human health. Long-term exposure to xylene environment will lead to adverse health effect including headaches, itchy skin, throat irritation, dermatitis, and fatigue.[4,5] Therefore, it is of great significance to construct high performance xylene sensors.

Cobalt oxide (Co_3O_4), as a representative p-type semiconductor material, has been widely used in the field of photocatalytic,[6] supercapacitor,[7] lithium battery,[8] and energy storage.[9] In addition, it is regarded as an ideal sensing material due to its multivalent characteristics and unique catalytic function.[10–12] However, the response value of n-type oxide semiconductor (Sn) is usually larger than that of p-type oxide semiconductor (Sp) with same morphologies.[13] To enhance the sensing properties of Co_3O_4, various effective strategies have been adopted, such as noble metal catalyst loading,[14] and functionalization of p–n heterointerfaces.[15]

Among them, metal ions doping is an effective method to achieve good sensing performance, because doping will not only decrease the average crystalline size, but also affect carrier concentration and catalytic activity of sensing materials, which are beneficial to the enhancement of the sensing performance of Co_3O_4 sensors.[16,17] For example, the sensor based on 6.0 at.% Fe-doped Co_3O_4 showed a enhanced response of 18.2 to 100 ppm xylene at 175 °C.[18] Flower-like Zn-doped Co_3O_4 was prepared by the solvothermal synthesis method. It exhibited higher gas response (52.3) to 100 ppm acetone compared with pristine Co_3O_4.[19] Therefore, it is necessary to further study hole modulation by doping as well as the corresponding sensing mechanism.

Herein, hierarchical flower-like pure Co_3O_4 and In-doped Co_3O_4 nanostructures are obtained via a one-step hydrothermal synthesis method. Gas-sensing performance tests show that 4 at.% In-doped Co_3O_4 sensor has ultra-high responses of 55.9 to 100 ppm xylene at 150 °C, which is almost 3.8 times higher than that of pure Co_3O_4. Furthermore, it also shows good selectivity and anti-humidity properties. Adjust the number of In ions in adsorption models, to analyze the changes of different structure models and adsorption energies. Combined with the DFT calculation results, the enhanced sensing mechanism is systematically studied.

2. Experimental detials

2.1. Preparation of pristine Co_3O_4 and In-doped Co_3O_4 nanostructures

Typically, 4 mmol of $Co(NO_3)_2{\cdot}6H_2O$ and 8 mmol of 2-methylimidazole were dissolved into 70 mL of methanol under magnetic stirring. Next, an amount of $In(NO_3)_3{\cdot}4.5H_2O$ was added to the mixed solution. The clear solution was transferred to a 100 mL teflon-lined stainless steel autoclave and heated at 120 °C for 4 h. Next the resulting precipitate was collected by centrifugation and washed by DI water and ethanol alternately several times, and then dried at 70 °C for 12 h. Finally,

†Corresponding author. E-mail: xiaoliang732@163.com
© 2023 Chinese Physical Society and IOP Publishing Ltd

the as-obtained samples were heated to 400 °C at the rate of 2 °C/min for 2 h. The products with In to Co molar ratios of 0%, 1%, 4% and 7% were labeled as Co_3O_4, In@Co_3O_4-1, In@Co_3O_4-4 and In@Co_3O_4-7, respectively.

2.2. Characterization

The structures were investigated by x-ray diffraction (XRD, Rigaku D/max-2500) with Cu-$K\alpha 1$ radication (λ = 1.54056 Å). The morphologies of the materials were determined by using scanning electron microscopy (SEM, Magellan-400), and detailed structural information was obtained by transmission electron microscopy (TEM, JEOL JEM-2200FS). UV spectroscopy (Shimadzu UV-2450) was used to analyze bandgap changes of synthesized materials. Specific surface areas were calculated by the Brunauer–Emmett–Teller (BET, Micromeritics ASAP 2420) method, and surface elemental composition was conducted by x-ray photoelectron spectroscopy (XPS, ESCALAB 250XI spectrometer).

2.3. Fabrication and measurement of gas sensor

The fabrication process of gas sensor has been described in our previous work.[20,21] Firstly, the sample powders were dispersed evenly in absolute ethanol by grinding to form the paste, which was then uniformly coated on a square ceramic plate. The back of the ceramic plate was loaded with a pair of Ru electrodes. Finally, the ceramic plate was welded to a hexapod base by Pt lead wires attached to four corners. The schematic diagram of the sensor is shown in Fig. S1 in the supplementary material.

A CGS-8 intelligent gas sensing analysis system (Beijing Elite Tech. Co., Ltd., China) was applied to measure the sensing performance of sensors, and the data acquisition interval was set to 1 s. The response of sensors was expressed as $S = R_g/R_a$, where R_g and R_a denoted the sensor resistance when exposed to target gas and air atmosphere, respectively. The response (t_{res}) and recovery (t_{rec}) times were defined as the time to reach 90% variation of the resistance after the sensor was exposed to the target gases and fresh air, respectively.[22]

2.4. Theory models

In this work, all the calculations were carried out using Vienna *ab initio* simulation package (VASP) within the framework of density functional theory (DFT).[23] We chose Co_3O_4 (311) surface and introduce different numbers of In atoms into the surface model by substituting Co with In, creating three theoretical models. According to the number of In atoms in the model, they are named as CI0, CI1, and CI5, respectively, the pristine structures and optimized structures are shown in Fig. S2 in the supplementary material. A cut-off energy of 500 eV was adopted to ensure the energy convergence, and the k-point grid of $3 \times 2 \times 1$ was set for geometry optimization.

To analyze the adsorption strength of xylene molecule with different models, the adsorption energy (E_{ads}) of xylene on Co_3O_4 surface was defined as

$$E_{ads} = E_{(\text{model+xylene molecule})} - E_{\text{model}} - E_{\text{xylene molecule}}, \quad (1)$$

where $E_{(\text{model+xylene molecule})}$, E_{model}, and $E_{\text{xylene molecule}}$ are the total energies for xylene molecule on the model, isolated model and single xylene molecule, respectively.[24]

3. Results and discussion

3.1. Structural and morphological characteristics

The XRD pattern of pristine and In-doped Co_3O_4 materials are exhibited in Fig. 1. All diffraction peaks of the as-obtained materials are ascribed to the cubic Co_3O_4 structure (JCPDS No. 74-2120). Moreover, no other peaks come from impurity phases are detected, indicating their high purity.[25] The pattern of (311) peaks of all the materials is shown in Fig. 1(b), which clearly reveals the peak of In-doped Co_3O_4 to be broader and shifted compared to that of the pure Co_3O_4. The lattice parameters of the four materials are calculated as shown in Table 1. Obviously, the slight shifts of the peak of In-doped Co_3O_4 to a lower angle can be observed compared with the pure Co_3O_4, showing the lattice expansion of Co_3O_4 when In ions are doped into Co_3O_4 because of their larger radius.[26,27]

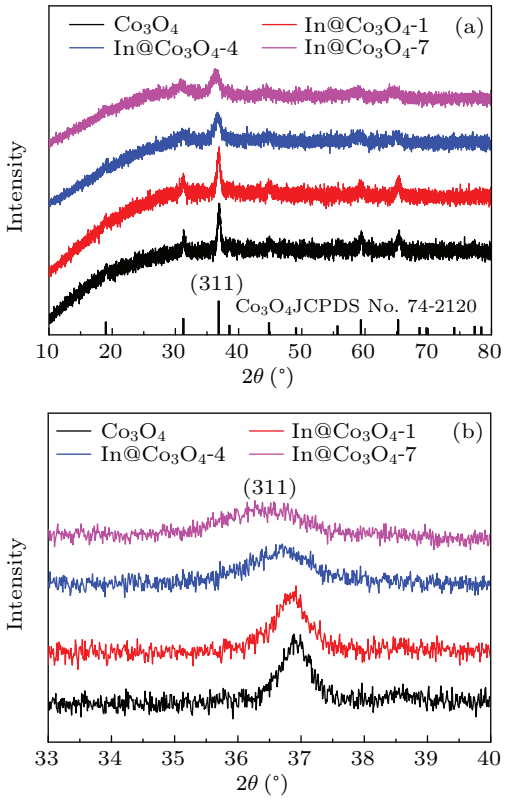


Fig. 1. XRD patterns (a) and high resolution (311) peaks (b) of the pure sample and of different In-dopant Co_3O_4 samples.

Table 1. Lattice parameters and crystal system of materials.

Materials	Crystal system	Lattice parameters					
		a (nm)	*b* (nm)	*c* (nm)	α	β	γ
Co_3O_4	Cubic	0.807	0.807	0.807	90°	90°	90°
In@Co_3O_4-1	Cubic	0.809	0.809	0.809	90°	90°	90°
In@Co_3O_4-4	Cubic	0.812	0.812	0.812	90°	90°	90°
In@Co_3O_4-7	Cubic	0.818	0.818	0.818	90°	90°	90°

The morphologies and structure of the pure Co_3O_4 and In@Co_3O_4-4 are observed by SEM and TEM, as shown in Figs. 2 and 3, respectively. Clearly, the hierarchical flower-like Co_3O_4 nanosphere is about 7 μm in diameter, and it can be seen that the nanosphere is assembled by many curving 2D nanosheets [Fig. 2(a)]. From Fig. 2(b), the nanosheets have porous structure. The TEM image [Fig. 2(c)] further reveals that these nanosheets contain many pores, which corresponds with SEM characterization. The formation of porous structure is caused by the release of surface adsorbed H_2O and volatile gas with the heating treatment.[19] Figure 2(d) shows a high-resolution TEM (HRTEM) image of pure Co_3O_4. The lattice spacing of 0.47 nm is attributed to the (111) plane of cubic Co_3O_4. Figures 3(a)–3(c) show the SEM and TEM images of In@Co_3O_4-4 nanosphere, which exhibit a similar flower-like nanostructure, which is composed of 2D porous nanosheets. In addition, it can be seen that the doping of In ions results in a significant decrease in the size of nanosheets.[28] The HRTEM image of the In@Co_3O_4-4 nanosphere shows the lattice spacing of 0.24 nm, which is ascribed to the (311) plane of Co_3O_4. Furthermore, the corresponding SEM and TEM images of In@Co_3O_4-1 and In@Co_3O_4-7 can be observed in Figs. S3 and S4, which exhibit a similar structure and pattern to In@Co_3O_4-4.

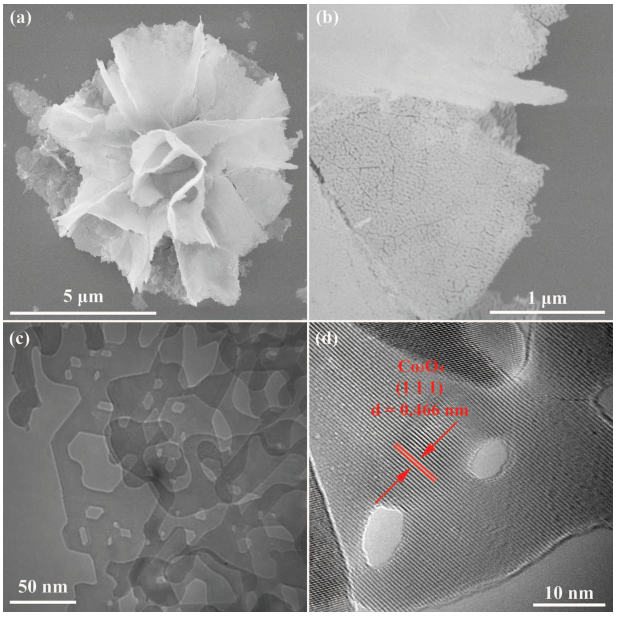


Fig. 2. [(a), (b)] SEM, (c) TEM, and (d) HRTEM images of pure Co_3O_4.

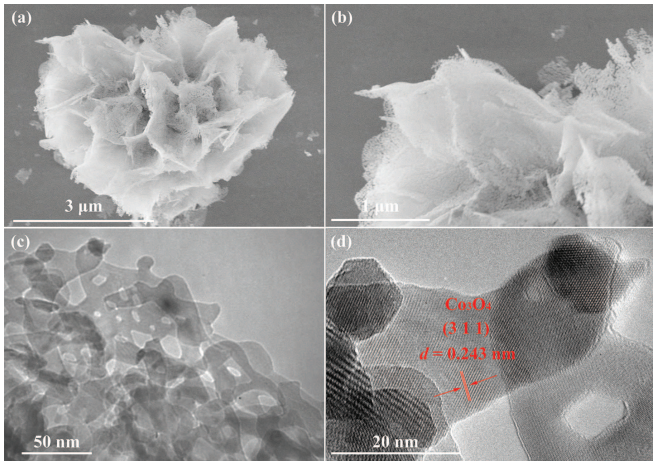


Fig. 3. [(a), (b)] SEM, (c) TEM, and (d) HRTEM images of In@Co_3O_4-4.

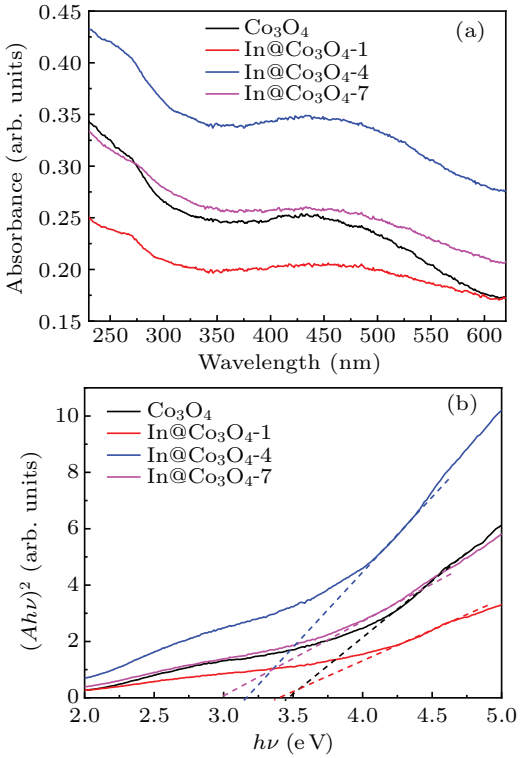


Fig. 4. UV-vis diffraction spectrum (a) and the plots of $(Ah\nu)^2$ versus $h\nu$ (b) of pure and In-doped Co_3O_4 samples.

The UV-visible absorption spectra of pure Co_3O_4 and In-doped Co_3O_4 [Fig. 4(a)] could reveal the bandgap (E_g), which can be described by the formula $(\alpha h\nu)^{1/n} = A(h\nu - E_g)$, where α is the absorption coefficient, h is the Plank constant, ν is the photon frequency, A is a constant related to the material, and n is the electronic transition parameter of 1/2 (direct bandgap semiconductor).[29] Therefore, E_g can be calcu-

lated by extrapolating the peak linear portion of the $(\alpha h\nu)^2$–$h\nu$ curve to the energy axis.[30] As shown in Fig. 4(b), E_g of Co_3O_4, In@Co_3O_4-1, In@Co_3O_4-4, and In@Co_3O_4-7 are 3.47 eV, 3.39 eV, 3.16 eV, and 2.97 eV, respectively. Since doped In ions substitute Co into Co_3O_4 lattice and form impurity energy levels below the conduction band edge, the adsorption edge shifts to lower energy, which benefits to carrier transmission.[31]

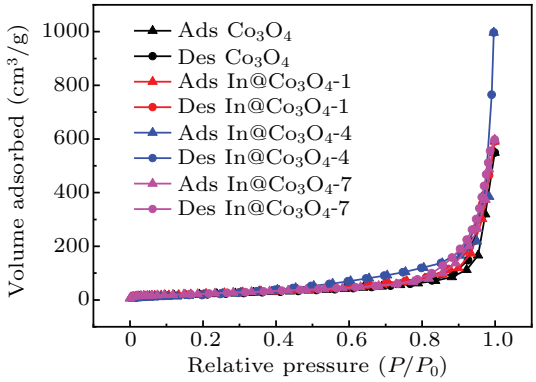


Fig. 5. The N_2 adsorption-desorption isotherms of pure and In-doped Co_3O_4 samples.

The specific surface areas of Co_3O_4, In@Co_3O_4-1, In@Co_3O_4-4, and In@Co_3O_4-7 are 101.6 m^2/g, 122.1 m^2/g, 149.9 m^2/g, and 131.4 m^2/g, respectively (Fig. 5). It is obvious that doping In ions effectively increases the specific surface area, and the specific surface area of In@Co_3O_4-4 is larger than that of other samples. The large specific surface area will obtain more abundant regions, which is helpful for enhancing gas responses.[32]

The chemical states and elemental composition of Co_3O_4, In@Co_3O_4-1, In@Co_3O_4-4, and In@Co_3O_4-7 samples are determined by XPS. The Co 2p spectra of In@Co_3O_4-4 shows two strong peaks at 795.1 eV and 779.7 eV, which correspond to Co $2p_{1/2}$ and Co $2p_{3/2}$, accompanied by two satellite peaks, as shown in Fig. 6(a). In addition, the peaks of Co $2p_{1/2}$ and Co $2p_{3/2}$ are composed of Co^{3+} and Co^{2+}.[33] Figure 6(b) exhibits the In 3d spectra of In@Co_3O_4-4. Two peaks are indexed as In $3d_{3/2}$ and In $3d_{5/2}$, respectively.[34] The Co 2p and In 3d spectra of In@Co_3O_4-1 and In@Co_3O_4-7 are shown in Fig. S5. Figures 6(c)–6(f) show the O 1s spectra of Co_3O_4, In@Co_3O_4-1, In@Co_3O_4-4, and In@Co_3O_4-7, respectively. It can be seen that the O 1s peak can be divided various parts including lattice oxygen (O_L), oxygen vacancy (O_V), and chemisorbed oxygen (O_C), respectively.[35] The relative percentages of each oxygen species of in the materials are exhibited in Table S1. Compared with other samples, In@Co_3O_4-4 possesses more oxygen vacancies and chemisorbed oxygen.

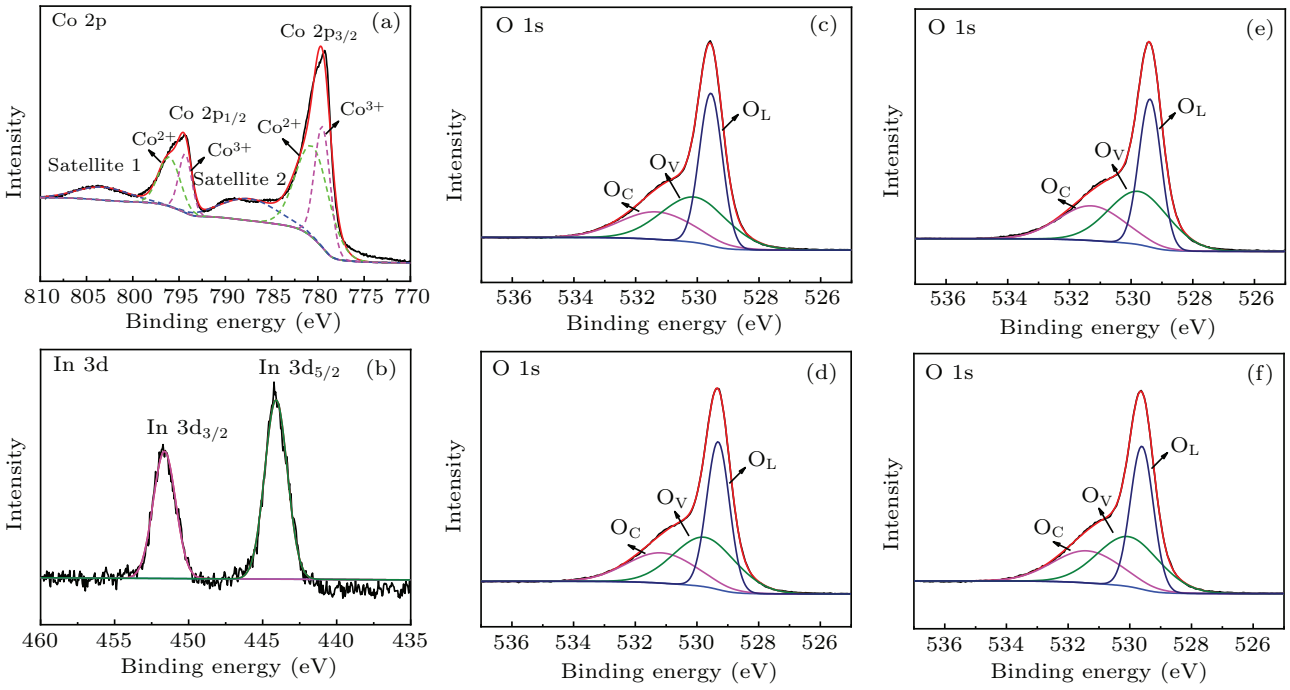


Fig. 6. XPS patterns of In@Co_3O_4-4: (a) Co 2p and (b) In 3d; (c)–(f) O 1s XPS spectra of pure Co_3O_4, In@Co_3O_4-1, In@Co_3O_4-4, and In@Co_3O_4-7, respectively.

3.2. Gas sensing properties

Operating temperature will seriously influence gas adsorption and desorption process.[36,37] Thus the response values of Co_3O_4 and In-doped Co_3O_4 samples to 100 ppm xylene at different temperature (from 130 to 170 °C) were measured [Fig. 7(a)]. The response values of all the products increase firstly and then decline rapidly with the increasing of temperature. An equilibrium between adsorption and desorption process is obtained at 150 °C, which leads to a maximum response value. In addition, the highest responses of In@Co_3O_4-

4 are about 55.9 (R_g/R_a), which are 3.78 times higher than that of Co_3O_4 (14.8). The excellent selectivity is important property for detecting gases in practical applications. The response of sensors to 100 ppm different gases (aniline, triethylamine, xylene, acetone, formaldehyde, methanol, ammonia and benzene) were investigated at 150 °C (Fig. 7(b)). Clearly, all the sensors exhibit higher responses to xylene than to other testing gases, and the In@Co_3O_4-4 has the highest response to xylene, indicating that it possesses outstanding selectivity for xylene.

The repeatability of sensors to 100 ppm xylene at 150 °C is exhibited in Fig. 7(c). The response maintains a substantially constant value upon six successive measurement, which demonstrates that the sensors present stable repeatability. To check the long-term stability, responses of the four sensors to 100 ppm xylene were recorded for a period of one month (Fig. 7(d)). It can be seen that the gas response values slightly decrease with the extension of time. This decreasing tendency may be caused by changes in ambient humidity, indicating that all the sensors have good long-term stability. The response of Co_3O_4 based samples to xylene with the concentration ranging from 1 to 200 ppm at 150 °C are shown in Fig. S6. All responses increase with increasing xylene concentration. Remarkably, the detection limit of these gas sensors can be as low as 1 ppm. In addition, the sensor based on In@Co_3O_4-4 shows the highest responses in these sensors.

Figure 8 presents the dynamic response-recovery curves of all the sensors. The response/recovery speed of Co_3O_4, In@Co_3O_4-1, In@Co_3O_4-4, and In@Co_3O_4-7 are 49 s/11 s, 38 s/57 s, 142 s/127 s, and 102 s/125 s, respectively. In addition, the sensor resistance increases with increasing the In doping amount. The phenomenon can be explained such that doping makes In ions occupy the site of Co ions, which leads to the increase of resistance.[38] Figure S7 shows the responses of all the sensors to 100 ppm xylene at different relative humidities (from 10% to 90%). It can be seen that no significant change can be detected in the four curves. The inherent anti-humidity characteristic of Co_3O_4[39] and the abundant defect oxygen in In@Co_3O_4 samples caused by In doping lead to the good anti-humidity performance.[40] As the water molecules would mainly be adsorbed at the defect sites of materials,[41] the less water vapor would compete with xylene gas.[42]

The comparison of xylene sensing properties between In@Co_3O_4-4 based sensor and other sensors is summarized in Table 2. In comparison of the responses (Res.) and operating temperature (Temp.), the In@Co_3O_4-4 sensor in this work possesses higher gas response and lower working temperature. Hence, it is expected to have excellent application prospects for xylene gas sensors.

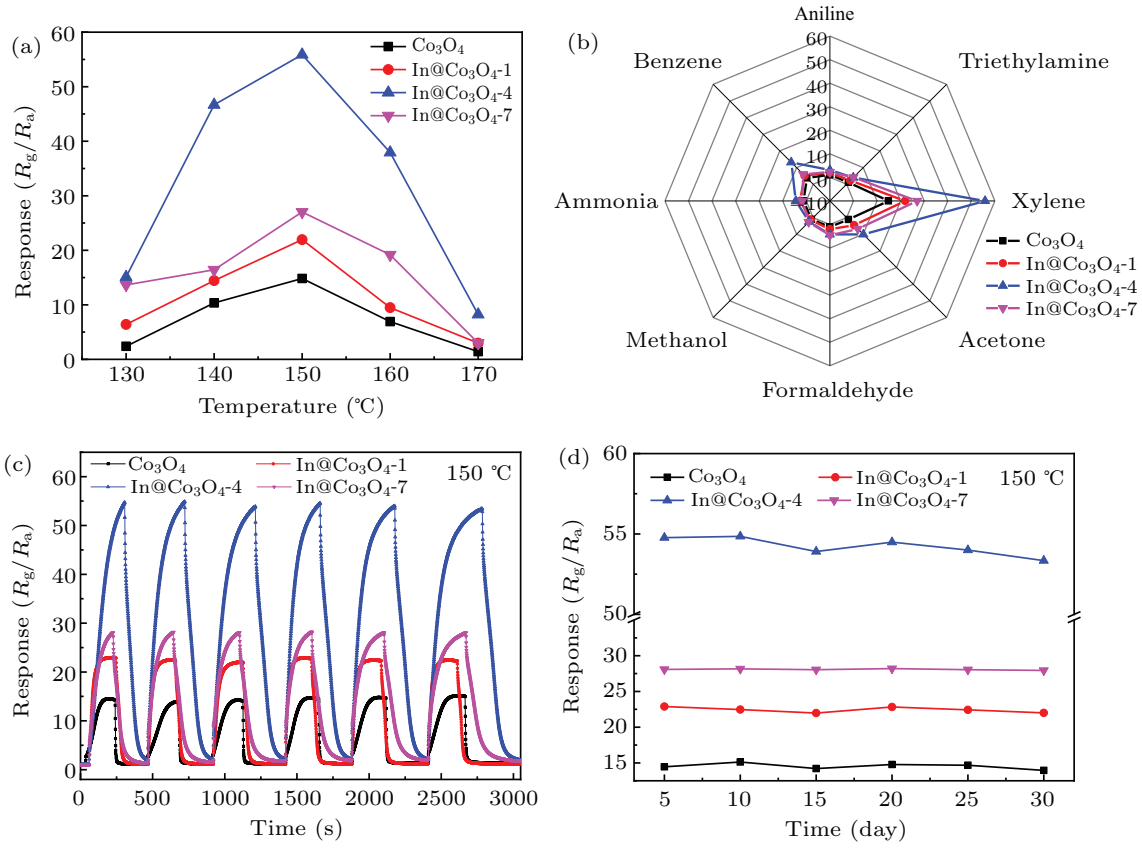


Fig. 7. (a) Response of sensors based on the pure and In-doped Co_3O_4 samples to 100 ppm xylene at different operating temperatures. (b) The response values of the sensors to 100 ppm different gases at 150 °C. (c) Six cycles of the dynamic response-recovery curve of the sensors to 100 ppm xylene. (d) Long-term stability of the sensors.

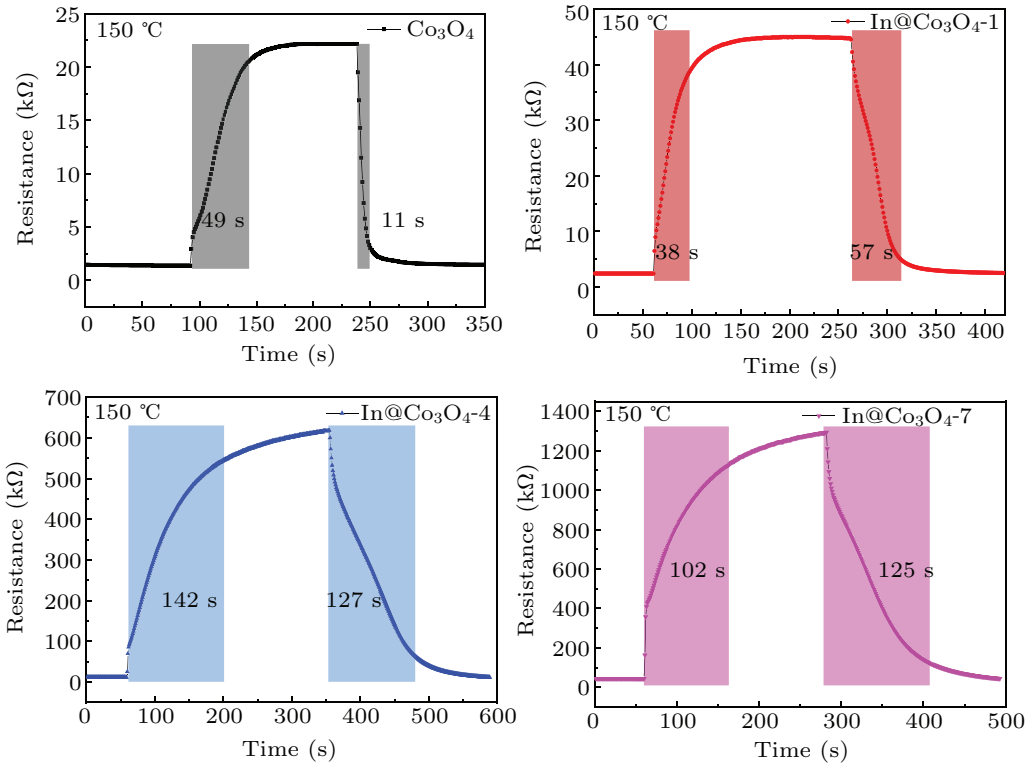


Fig. 8. The response/recovery speed of (a) pure Co_3O_4, (b) In@Co_3O_4-1, (c) In@Co_3O_4-4, and (d) In@Co_3O_4-7 to 100 ppm xylene 150 °C.

Table 2. Comparison of xylene-sensing performances of the sensors based different materials.

Materials	Temp. (°C)	Conc. (ppm)	Res.
5Zr-MoO_3[5]	206	100	7.99
6 at.% Fe-doped Co_3O_4[18]	175	100	18.2
0.5 wt% Ag/TiO_2 nanorod[43]	375	100	6.5
3 at.% Sn-doped NiO[44]	225	100	20.2
W-doped NiO[45]	375	200	8.74
In@Co_3O_4-4	150	100	55.9

3.3. Gas sensing mechanism

Gas sensing mechanism of Co_3O_4 belongs to surface control model.[17] When Co_3O_4 or In-doped Co_3O_4 based sensor is exposed to air, Co_3O_4 surface will adsorb oxygen molecules and form oxygen species (O_2^-, O^- and O^{2-}) by capturing free electrons from conduction.[46,47] Therefore, a hole accumulation layer will be formed and the sensor resistance will decline. Subsequently, when the sensor transfer into the xylene atmosphere, the xylene molecules will react with O^-. Thus the electrons will be released back to the conduction band of sensing material and neutralizing the holes (Fig. 9), resulting in a rise in electrical resistance. These reactions can be expressed as

$$O_2^-(\text{ads}) + e^- \rightarrow 2O^-(\text{ads}), \tag{2}$$

$$C_8H_{10} + 21O^-(\text{ads}) \rightarrow 8CO_2 + 5H_2O + 21e^-, \tag{3}$$

$$e^- + h^+ \rightarrow \text{null}. \tag{4}$$

The experimental results show that the In-doped Co_3O_4 based sensor exhibit better sensing properties, which can be explained as follows. Because of doping, In ion will occupy the site of the divalent Co ion and form a positive substituted cation ($In_{Co}^{\cdot}$). At the same time, the unbalanced charges can be compensated for by the generation of two electrons and oxygen gas or by the formation of Co vacancies ($V_{Co}^{\cdot\cdot}$):[27]

$$In_2O_3 \xrightarrow{CoO} 2In_{Co}^{\cdot} + 2e^- + 2O_O^X + \frac{1}{2}O_2\,(\text{gas}), \tag{5}$$

$$In_2O_3 \xrightarrow{CoO} 2In_{Co}^{\cdot} + 3O_O^X + V_{Co}^{\cdot\cdot}. \tag{6}$$

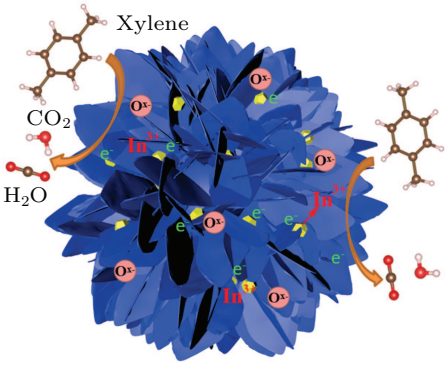


Fig. 9. Schematic diagram of the In-doped Co_3O_4 sensor when exposed to xylene.

As a result, electrons are generated to neutralize holes in the In-doped Co_3O_4 sample and increase the resistance. In the previous report,[2] the same number of electrons injected into p-type semiconductor oxide material in the sensing reaction would result in a higher variation in sensor resistance with the lower hole concentration, which leads to increased gas response. In addition, the oxygen vacancy (O_V) proportion

(36.6%) of In@Co_3O_4-4 is higher than that of other samples (Table S1). It is reported that a larger amount of O_V can offer more active regions for redox reaction, which enhance sensing performances of the gas sensor.[48,49]

In addition, the surface area of In@Co_3O_4-4 is higher than that of pure Co_3O_4, indicating that the In@Co_3O_4-4 based sensor possesses more chemisorbed oxygen species, which leads to higher responses.[50]

To further discuss the sensing mechanism, we analyze the adsorption strength of Co_3O_4 models containing different amounts of In ions for xylene molecule. As shown in Fig. 10, compared with the CI0 and CI5 models, the atomic position change near the adsorption interface of CI1 model is most obvious, indicating that the CI1 model has the strongest interaction with xylene. In addition, the adsorption energies between the three adsorption models and xylene molecule are listed in Table 3. It is obvious that the adsorption energy of CI1 is lower than other models, proving that the CI1 model is easier to adsorb xylene molecules.[21] With the increasing number of In ions, the adsorption energy increases first and then decreases, which is consistent with the experimental results.

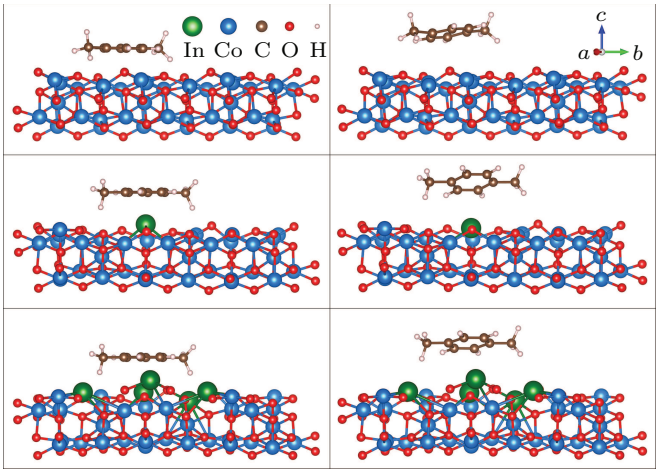


Fig. 10. The initial and optimized structures of three different adsorptive configurations to xylene molecule: [(a), (b)] CI0, [(c), (d)] CI1, and [(e), (f)] CI5.

Table 3. The adsorption energies between different models and xylene molecule.

Model	CI0	CI1	CI5
Adsorption energy (eV)	–0.08	–0.43	–0.12

4. Conclusion

In summary, we have prepared hierarchical flower-like pure and In-doped Co_3O_4 nanostructures by employing a one-step hydrothermal synthesis method. The results of sensing measurement illustrate that In@Co_3O_4-4 based sensor presents the best gas sensing performance at low optimum operating temperature (150 °C). The enhanced gas sensing performance is ascribed to the doping of In ions, which could increase specific surface area, carrier concentration, and the content of oxygen vacancies. In addition, the DFT analysis verifies the experimental results, demonstrating that an appropriate doping of In ions is helpful for improving the adsorption strength of xylene molecules. As described above, the In-doped Co_3O_4 sensor has great potential for xylene detection.

References

[1] Liu W J, Wei D D, Zhao X Y, Xiao F and Yang C 2022 *Appl. Surf. Sci.* **602** 154301
[2] Qiu L, Zhang S D, Huang J B, Wang C H, Zhao R Y, Qu F D, Wang P and Yang M H 2020 *Sens. Actuators B:-Chem.* **308** 127520
[3] Guo M M, Luo N, Chen Y, Fan Y, Wang X H and Xu J Q 2022 *J. Hazard. Mater.* **429** 127471
[4] Kim T H, Kwak C H and Lee J H 2017 *ACS Appl. Mater. Interfaces* **9** 32034
[5] Li X, Jiang D S, Fan Y Z, Zhang N, Liu C X, Adimi S, Zhou J R, Wen S P and Ruan S P 2020 *Inorg. Chem. Front.* **7** 1704
[6] Magdalane C M, Kaviyarasu K, Arularasu M V, Kanimozhi K and Ramalingam G 2019 *Surf. Interfaces* **17** 100369
[7] Sagadevan S, Marlinda A R, Johan M R, Umar A, Fouad H, Alothman O Y, Khaled U, Akhtar M S and Shahid M M 2019 *J. Colloid Interface Sci.* **558** 68
[8] Eom W, Kim A, Park H, Kim H and Han T H 2016 *Adv. Funct. Mater.* **26** 7605
[9] Sriram B, Sathiyan A, Wang S F, Elanthamilan E, Joseph X B, Baby J N, Merlin J P and Ezhilarasi J C 2021 *J. Solid State Chem.* **295** 121931
[10] Chen X H, Liang R, Qin C, Ye Z Z and Zhu L P 2022 *J. Alloys Compd.* **891** 161868
[11] Xu J M and Cheng J P 2016 *J. Alloys Compd.* **686** 753
[12] Zhou T T, Zhang T, Zhang R, Lou Z, Deng J A and Wang L L 2017 *Appl. Surf. Sci.* **426** 951
[13] Hübner M, Simion C E, Tomescu-Stănoiu A, Pokhrel S, Barsan N and Weimar U 2011 *Sens. Actuators B:-Chem.* **153** 347
[14] Molavi R and Sheikhi M H 2018 *Mater. Lett.* **233** 74
[15] Gao J Y, Hou M, Yang L, Guo S H and Xu K 2022 *Appl. Surf. Sci.* **605** 154769
[16] Sun H M, Tang X N, Zhang J R, Li S and Liu L 2021 *Sens. Actuators B:-Chem.* **346** 130546
[17] Cheng P F, Dang F, Wang Y L, Gao J N, Xu L P, Wang C, Lv L, Li X, Zhang B and Liu B J 2021 *Sens. Actuators B:-Chem.* **328** 129028
[18] Zhang N, Qin Q X, Ma X H, Zhou J R, Sun L, Chen C, Wen S P, Chen Y and Ruan S P 2017 *J. Alloys Compd.* **723** 779
[19] Li K, Chang X, Qiao X R, Yu S F, Li X F, Xia F J and Xue Q Z 2021 *Appl. Surf. Sci.* **565** 150520
[20] Yang T Y, Gu K K, Zhu M M, Lu Q, Zhai C B, Zhao Q, Yang X D and Zhang M Z 2019 *Sens. Actuators B:-Chem.* **279** 410
[21] Liang X, Zhang J, Zhang K W, Yang X D and Zhang M Z 2022 *Inorg. Chem. Front.* **9** 259
[22] Wang S Q, Xie J, Hu J D, Qin H Y and Cao Y L 2020 *Appl. Surf. Sci.* **512** 145722
[23] Zeng W, Li Y Q, Miao B, Lin L Y and Wang Z C 2014 *Sens. Actuators B:-Chem.* **191** 1
[24] Feng C, Qin H B, Luan X H, Kuang T F and Yang D G 2018 *Chem. Phys. Lett.* **706** 355
[25] Du L Y, Sun H M and Liu Y 2022 *J. Alloys Compd.* **900** 163470
[26] Li P P, Cao C Y, Shen Q K, Bai B, Jin H Q, Yu J, Chen W M and Song W G 2021 *Sens. Actuators B:-Chem.* **339** 129886
[27] Tong B, Meng G, Deng Z H, Gao J J, Liu H Y, Dai T T, Wang S M, Shao J Z, Tao R H, Kong F T, Tong W, Luo X and Fang X D 2021 *J. Alloys Compd.* **851** 155760
[28] Qiu L, Zhang S D, Huang J B, Wang C H, Zhao R Y, Qu F D, Wang P and Yang M R 2020 *Sens. Actuators B:-Chem.* **308** 127520
[29] Mao J N, Hong B, Chen H D, Gao M H, Xu J C, Han Y B, Yang Y T, Jin H X, Jin D F, Peng X L, Li J, Ge H L and Wang X Q 2020 *J. Alloys Compd.* **827** 154248
[30] Niu J Y, Wang L, Hong B, Xu J C, Han Y B, Jin H X, Zeng Y X, Peng X L, Ge H L and Wang X Q 2021 *Nanotechnology* **32** 485502
[31] Li X Q, Wei J Q, Xu J C, Jin H X, Jin D F, Peng X L, Hong B, Li J, Yang Y T, Ge H L and Wang X 2017 *J. Nanopart. Res.* **19** 396

[32] Wang Z H, Tian Z W, Han D M and Gu F B 2016 *ACS Appl. Mater. Interfaces* **8** 5466

[33] Tong Y, Mao H N, Xu Y L and Liu J Y 2019 *Inorg. Chem. Front.* **6** 2055

[34] Xie J Y, Liu X H, Jing S L, Pang C, Liu Q S and Zhang J 2021 *ACS Appl. Mater. Interfaces* **13** 39621

[35] Wang S, Huang D, Xu S S, Jiang W K, Wang T, Hu J, Hu N T, Su Y J, Zhang Y F and Yang Z 2017 *Phys. Chem. Chem. Phys.* **19** 19043

[36] Zhang R, Gao S, Zhou T T, Tu J C and Zhang T 2020 *Appl. Surf. Sci.* **503** 144167

[37] Navale Y H, Navale S T, Stadler F J, Ramgir N S and Patil V B 2019 *Ceram. Int.* **45** 1513

[38] Kim H J, Choi K I, Kim K M, Na C W and Lee J H 2012 *Sens. Actuators B:-Chem.* **171–172** 1029

[39] Fan X X, Wang J F, Sun C L, Huang C, Lu Y J, Dai P, Xu Y J and He W M 2022 *RSC Adv.* **12** 19384

[40] Yang Q Y, Wang Y L, Liu J, Liu J Y, Gao Y, Sun P, Jie Z, Zhang T, Wang Y and Lu G Y 2017 *Sens. Actuators B:-Chem.* **241** 806

[41] Kim J, Hou B, Park C, Bum Bahn C, Hoffman J, Black J, Bhattacharya A, Balke N, Hong H, Kim J H and Hong S 2017 *Sci. Rep.* **7** 1

[42] Cheng P F, Dang F, Wang Y L, Gao J N, Xu L P, Wang C, Lv L, Li X, Zhang B and Liu B J 2021 *Sens. Actuators B:-Chem.* **328** 129028

[43] Zhang Y Q, Bai J H, Zhou L S, Liu D Y, Liu F M, Liang X S, Gao Y, Liu F M, Yan X and Lu G Y 2019 *J. Colloid Interface Sci.* **536** 215

[44] Gao H Y, Wei D D, Lin P F, Liu C, Sun P, Shimanoe K, Yamazoe N and Lu G Y 2017 *Sens. Actuators B:-Chem.* **253** 1152

[45] Feng C H, Wang C, Zhang H, Li X, Wang C, Cheng P F, Ma J, Sun P, Gao Y, Zhang H, Sun Y F, Zheng J and Lu G Y 2015 *Sens. Actuators B:-Chem.* **221** 1475

[46] Qiao J P, Zhu Z P, Yan X Y and Qin J M 2012 *Chin. Phys. Lett.* **29** 020701

[47] Bai S L, Tian K, Tian Y, Guo J, Feng Y J, Luo R X, Li D Q, Chen A F and Liu C C 2018 *Appl. Surf. Sci.* **435** 384

[48] Yan W J, Hu M, Liang J R, Wang D F, Wei Y L and Qin Y X 2016 *Chin. Phys. B* **25** 040702

[49] Hu J, Xiong X Q, Guan W W, Long H Z, Zhang L X and Wang H H 2022 *Sens. Actuators B:-Chem.* **361** 131705

[50] Liu H, Chen J J, Wang Y, Xiong S C, Su Z, Wang Y, Yang W H, Chu X F, Yang W N, Peng Y, Si W Z and Li J H 2021 *Chem. Eng. J.* **414** 128643